Exp Fluids (2009) 47:119–134
DOI 10.1007/s00348-009-0643-4

RESEARCH ARTICLE

Quantitative X-ray measurements of high-pressure fuel sprays from a production heavy duty diesel injector

A. I. Ramírez · S. Som · Suresh K. Aggarwal · A. L. Kastengren · E. M. El-Hannouny · D. E. Longman · C. F. Powell

Received: 15 August 2008 / Revised: 5 March 2009 / Accepted: 9 March 2009 / Published online: 25 March 2009

Abstract A quantitative and time-resolved X-ray radiography technique has been used for detailed measurements of high-pressure fuel sprays in the near-nozzle region of a diesel engine injector. The technique provides high spatial and temporal resolution, especially in the relatively dense core region. A single spray plume from a hydraulically actuated electronically controlled unit injector model 315B injector with a 6-hole nozzle was isolated and studied at engine-like densities for two different injection pressures. Optical spray imaging was also employed to evaluate the effectiveness of the shield used to isolate a single spray plume. The steady state fuel distributions for both injection pressures are similar and show a dense spray region along the axis of the spray, with the on-axis spray density decreasing as the spray progresses downstream. The higher injection pressure case exhibits a larger cone angle and spray broadening at the exit of the nozzle. For some time periods, the near-nozzle penetration speed is lower for the high injection pressure case than the low injection pressure case, which is unexpected, but can be attributed to the needle and flow dynamics inside the injector causing slower pressure build-up for the former case. Rate of injection testing was performed to further understand near-nozzle behavior. Mass distribution data were obtained and used to find mass-averaged velocity of the spray. Comparisons of the radiography data with that from a common rail single-hole light duty injectors under similar injection conditions show several significant differences. The current data show a larger cone angle and lower penetration speed than that from the light-duty injector. Moreover, these data display a Gaussian mass distribution across the spray near the injector, whereas in previous light-duty injector measurements, the mass distribution had steeper sides and a flatter peak. Measurements are also used to examine the spray models in the STAR-CD software.

A. I. Ramírez · S. Som · S. K. Aggarwal (✉)
Department of Mechanical and Industrial Engineering, University of Illinois at Chicago, 842 W. Taylor/MC 251, Chicago, IL 60607, USA
e-mail: ska@uic.edu

A. L. Kastengren · E. M. El-Hannouny · D. E. Longman · C. F. Powell
Energy Systems Division, Argonne National Laboratory, 9700 S. Cass Avenue, Argonne, IL 60439, USA

1 Introduction

Diesel engines have been the preferred power train for heavy-duty applications, especially in trucks, due to their high efficiency and high power density. During the last decade, the innovation in high-pressure direct injection combined with turbo-charging techniques has revolutionized the diesel engine technology. Despite these advances, heavy-duty diesel engines intrinsically generate high soot and NOx emission, which need to be reduced in order to fulfill the emission legislations worldwide. Fuel injection characteristics, in particular the atomization and penetration of the fuel, are known to affect NOx and particulate

formation in diesel engines (Pierpont and Reitz 1995; Montgomery et al. 1996).

Improved fuel/air mixing can lead to more efficient combustion and lower particulate emissions. The mixing process is governed by injection and spray processes. The injection characteristics depend on factors such as the needle lift dynamics and inner nozzle flow behavior, while the spray processes are influenced by aerodynamics outside the nozzle. Significant work has been done on characterizing the influence of various injection parameters such as nozzle orifice geometry, injection and ambient pressure, etc., on spray development (Pierpont and Reitz 1995; Montgomery et al. 1996; Han et al. 2002; Wang et al. 2003; Gavaises et al. 2006; Giannadakis et al. 2008). Establishing correlations between near-nozzle flow behavior and diesel engine performance and emissions will augment the capability of designing more efficient diesel engines. Detailed experimental data not only lead to further understanding of the spray behavior from the injector, but also provide valuable knowledge to enhance computational modeling capabilities.

Optical diagnostics have been extensively used to characterize diesel sprays. Siebers (1998) used Mie-scattered light imaging to perform extensive studies of diesel sprays with varied injection pressures, nozzle geometry, and ambient conditions. It was observed that the liquid length of the spray is more sensitive to ambient conditions (gas density and temperature) rather than the nozzle geometry and injection pressure. Arcoumanis et al. (1990) used laser techniques to investigate diesel sprays from multi-hole injectors, and observed spray tip penetration and velocity to be dependent on the frequency of injection. However, optical methods while providing valuable information have intrinsic limitations. Because of the high density of the droplets near the nozzle, most optical methods are ineffective in this area. Visible light is scattered by the dense fuel, thus causing the measurements to be ineffective until far downstream from the nozzle. Consequently, for typical high-speed sprays resulting from a diesel fuel injector, it is difficult to obtain information with sufficient time and spatial resolution, since high spray density near the nozzle prevents the acquisition of such data.

In recent years, X-ray radiography, a measurement technique based on X-ray absorption, has been well-established. Since the main interaction between the fuel and the X-rays is absorption, rather than scattering, the technique offers an appealing alternative to optical techniques for studying fuel sprays, especially in the dense near-nozzle region. While both X-ray radiography and optical images can provide global spray characteristics like penetration and cone angle, the X-ray technique provides quantitative data with high spatial and temporal resolutions. The X-ray radiography is perhaps the only technique that allows for measurement of the fuel mass distribution in the spray, permitting analyses that cannot be performed using optical spray data.

This X-ray radiography technique has been used previously to analyze the spray characteristics for single-hole research nozzles injecting into ambient pressure lower than typical of diesel engines (Kastengren et al. 2007a, b; Yue et al. 2001; Cheong et al. 2004; Powell et al. 2003). The use of higher pressure was restricted by design limitations of the X-ray windows and significant X-ray extinction caused by the fill gas (Ciatti et al. 2004; Powell et al. 2003). While these lower pressure experiments provide useful insights into the spray development characteristics, the effects of injecting into gas at heavy-duty engine-like density has not been investigated in previous studies.

Multi-hole nozzles are commonly used to improve the mixing in the engine cylinder. Spray from a multi-hole nozzle differs from that of a single-hole nozzle due to internal flow differences inside the nozzle. Soteriou et al. (1995) investigated cavitation in nozzles using large-scale and standard nozzles. The onset of cavitation in the nozzle was found to be asymmetrical and eventually propagates down the orifice and fills the hole. Increased turbulence was also found in the case of multiple holes over single holes. Chaves et al. (1995) performed studies of fuel spray using a real-scale transparent nozzle using optical techniques. Payri et al. (2008a, b) used optical techniques to examine the global spray behavior in the first 15 mm of the spray from a non-isolated 6-hole common rail injector. The spray tip penetration in the transient region was observed to behave differently than in the steady state region. Application of X-ray radiography to multi-hole nozzles is quite challenging due to the difficulty of obtaining adequate spray isolation. It is desired that only a single plume of interest sprays freely in the direction normal to the X-ray beam without interference from neighboring spray plumes. This requires significant design considerations. Leick et al. (2007) used a multi-hole, common rail, single fluid injection system where a single plume was isolated and investigated spray behavior using X-ray radiography under ambient density conditions corresponding to those in a typical automobile engine. They used a near production nozzle to investigate the spray from three orifices at two different gas densities, and observed that the ambient density has a relatively small effect on the mass distribution. In addition, the mass distributions obtained in this study indicated the absence of a pure liquid core in the spray, suggesting rapid mixing of gas and liquid near the nozzle.

The present study uses X-ray radiography technique to explore the near-nozzle region of a production multi-hole injector, and obtain quantitative measurements of high-pressure nonevaporating sprays at heavy-duty diesel engine-like densities. The entire spray event, including the

transient region of the spray where needle lift plays a significant role in fuel penetration is investigated. It focuses on the isolation of a single spray plume of a full production 6-hole injector in order to obtain data in the near-nozzle region. Geometry deviations, surface irregularities, and production flaws can all affect the operation of the injector. A production nozzle includes these effects and provides a more realistic representation of actual spray events. In addition, the use of a production nozzle facilitates direct correlations between X-ray spray studies and subsequent engine performance and emission investigations using the same injector and nozzle tip. In the present experiments, the geometrical effects of multiple holes are preserved by employing a specially designed isolation shield. This shield enables line-of-sight measurement of the plume of interest by deflecting the remaining five spray plumes. This technique therefore allows a more accurate study of the spray as it exits the nozzle.

While many experimental techniques have provided global spray characteristics such as cone angle and penetration, X-ray radiography is also able to measure the mass distribution in the spray, especially near the nozzle exit. This comprehensive experimental data can be used for the validation and further improvements in the spray models. Also from a modeling perspective, non-evaporating sprays provide a more stringent test for liquid breakup and atomization models in the near-nozzle region, since the uncertainties related to reacting flow models (such as evaporation, ignition, combustion, etc.) can be isolated. Some recent studies have attempted to use X-ray data for spray model validation. Tanner et al. (2004, 2006) employed a Cascade atomization and droplet breakup (CAB) model and compared the liquid penetration and transverse mass distribution with X-ray measurements. However, the rate of injection (ROI) profile was not known for injection conditions and injection velocities were determined by an iterative process to match the spray penetration. In the present study, the ROI was determined from a Bosch rate meter coupled with X-ray measurements, thus reducing the uncertainty associated with injection velocities.

To the best of our knowledge, the present study reports the first detailed evaluation of a full production multi-hole nozzle under engine-like ambient densities, and provides quantitative measurements in the near-nozzle region using X-ray radiography. Measurements include spray shape and liquid penetration as function of time, spray cone angle, ROI profile, as well as liquid mass distribution and spray velocity. These measurements are also used to examine the spray models in a CFD software STAR-CD. The current investigation thus further expands the available data for the validation and improvement of nonevaporating spray models that are currently used in diesel spray simulations.

2 Experimental setup

2.1 X-ray absorption

The X-ray measurements were performed at Argonne National Laboratory using the Advanced Photon Source (APS) facility, which generates a highly intense X-ray beam (approximately 4×108 photons/s). The X-ray radiography technique is based on the absorption of the monochromatic X-ray beam passing through the spray. The monochromaticity of the beam allows a straightforward application of the Beer–Lambert law relating the measured X-ray intensities to the mass of the fuel in the path of the beam, expressed as

$$\frac{I}{I_0} = \mathrm{e}^{-\mu M} \tag{1}$$

here μ is the absorption coefficient of the fuel in $mm^2/\mu g$, M the projected density of the fuel in the beam path in $\mu g/mm^2$, and I and I_0 the X-ray intensities during and before the spray event, respectively.

Schematic and top-view image of the experimental setup are shown in Fig. 1. The X-ray energy of 8 keV with a narrow range (2% bandwidth) of X-ray wavelengths was selected using a monochromator. This energy provides a good compromise between absorption and penetrating power, allowing significant absorption due to the spray while maintaining sufficient intensity through the spray chamber. Vertical and horizontal X-ray slits were used to limit the beam size. Full width half maximum (FWHM) values of the beam size were 260 μm in the axial direction and 50 μm in the transverse direction.

An avalanche photodiode (APD) with a time response faster than 5 ns is used to monitor the X-ray intensity. The APD output, which is proportional to the X-ray intensity, was recorded using a fast digitizing oscilloscope every 1 ns for a duration of 4 ms, which encompasses the entire spray event. At each position, the X-ray intensity from 128 successive spray events was averaged at every measurement position in order to improve signal to noise ratio. The time-resolved behavior of the spray is maintained as the sprays are averaged. Data were recorded, and Eq. 1 was then used to convert the X-ray intensity to projected density in the spray. X-ray measurements are a projection of the three-dimensional fuel density along the X-ray beam path, giving units of mass per unit area. The standard deviation of measurement is approximately 1.1 $\mu g/mm^2$, or 2.5%, based on a mean value of 45 $\mu g/mm^2$. The positioning of the nozzle is accurate to within about 3–5 microns in the vertical direction and 10–20 microns in the horizontal direction. More detailed descriptions of the technique can be found in other works (Kastengren et al. 2007a, b; Powell et al. 2001; Yue et al. 2001).

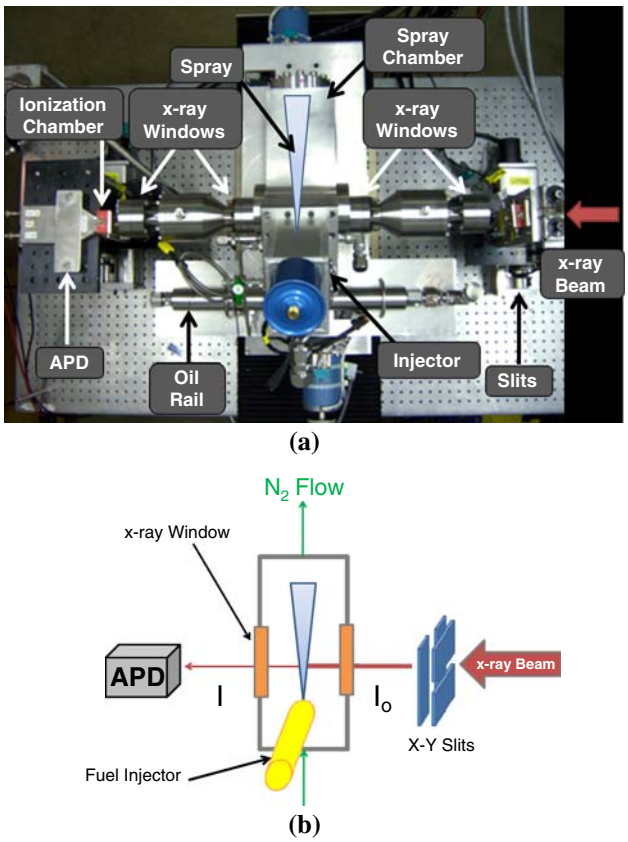

Fig. 1 **a** Top view image of experimental setup at APS, **b** schematic of experimental setup

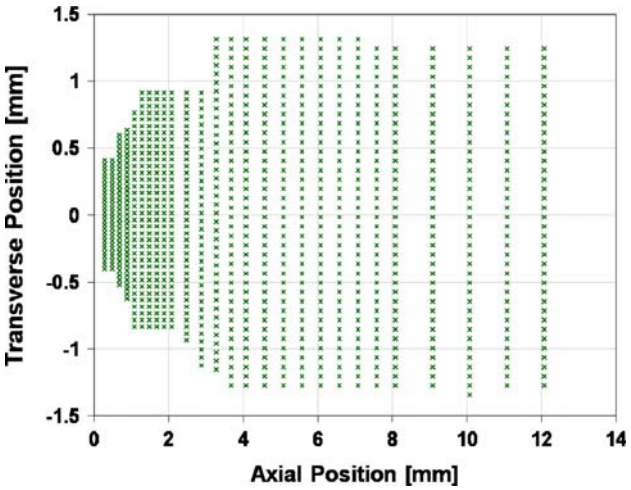

Fig. 2 Measurement grid showing the position of the X-ray beam in the line-of-sight coordinate system of the spray

The spray chamber was mounted on high-precision translation stages that moved it in two dimensions in the plane perpendicular to the X-ray beam. For each measurement condition, measurements were made at approximately 980 spatial locations. Figure 2 shows the measurement grid used in these experiments. The spatial resolution of the measurement is a function of both the size of the X-ray beam and the spacing between successive measurement points. The size of the X-ray beam is 260 μm × 50 μm. The spacing between measurement points varies across the measurement domain. Closest to the nozzle, measurements were taken each 0.2 mm in the axial direction and 0.03 mm in the transverse direction, eventually progressing to 1 mm axial and 0.07 transverse separation further downstream. It should be noted that these measurements are composite data from many different spray events. Thus, the radiography data show the persistent, ensemble average features of the spray, rather than the details of any particular spray event.

2.2 Injection system

In the present experiments a Caterpillar 315B hydraulically actuated electronically controlled unit injector (HEUI) was used. Unlike other injection systems, the HEUI 315 B requires both engine oil and fuel for operation. The HEUI injection system uses hydraulic pressure from the oil to raise the fuel pressure to the desired level for direct injection. This is done by an internal differential piston, which multiplies the relatively modest oil rail pressure to a high fuel injection pressure. This injector uses a pressure intensification ratio of approximately 6.6 between the oil rail pressure and injection pressure. Parameters such as the injection timing, duration, and quantity are controlled by a solenoid that is connected to the engine's Electronic Control Unit (ECU) (Yudanov 1995). More detailed description of the HEUI injection system can be found in (Mulemane et al. 2004; Glassey et al. 1993; Stockner et al. 1993).

2.3 Spray isolation

The full-production, mini-sac nozzle investigated in this study is shown schematically in Fig. 3a. It has six cylindrical holes each with a diameter of 169 μm separated by 126°. One orifice was carefully isolated in order to study the dynamics of a single spray plume. An isolation shield, shown in Fig. 3b deflected the remaining plumes, allowing the plume of interest to spray freely through the spray chamber in the direction indicated. Figure 3c provides a closer view of the isolation shield and the single hole in the opening. This isolation shield was designed in such a way that it does not block the remaining plumes; rather it deflects them after they emerge from the orifice without restriction.

The use of a full-production six-orifice injector is an advantage of this work since it represents equipment that is physically used in an engine. Because of the line-of-sight

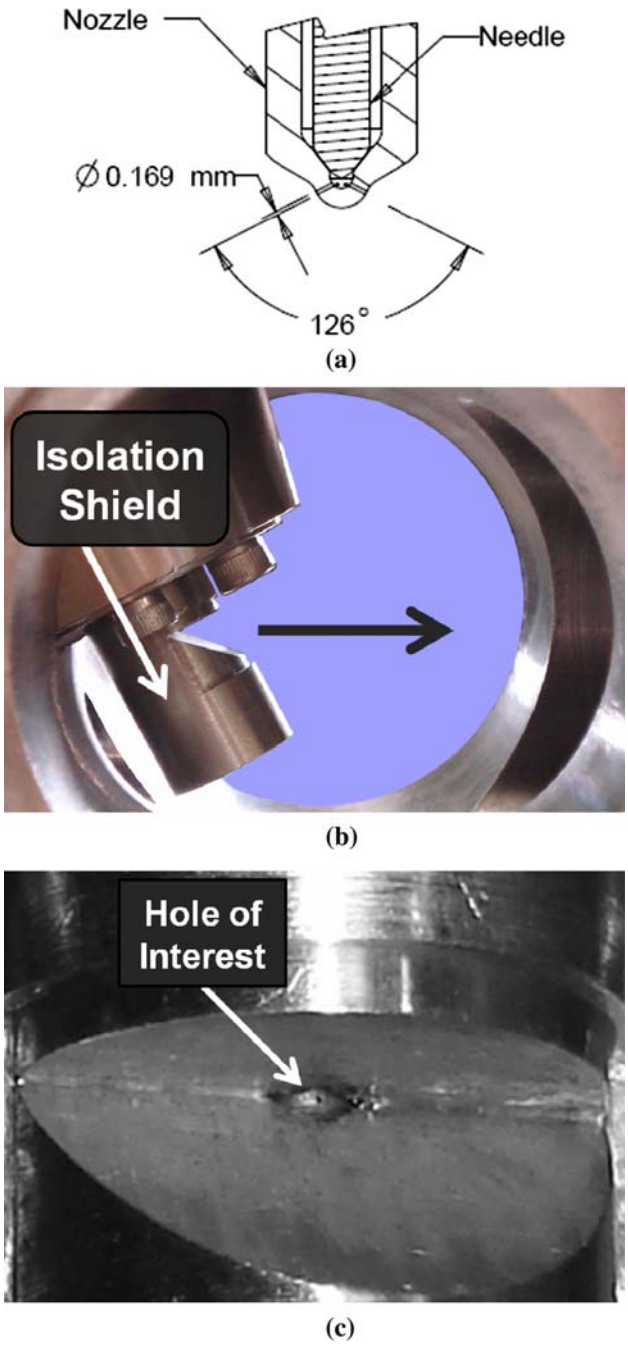

Fig. 3 **a** Schematic of injector nozzle tip, **b** isolation shield with arrow indicating direction of spray, the direction of the X-ray beam would be going into the plane of the page. **c** Zoomed image of nozzle tip and hole of interest in isolation shield

nature of the X-ray technique, spray plumes that are not desired for measurement must be removed from the measurement domain. This has been done in the past by plugging orifices adjacent to the plume-of-interest. Using an isolation shield to deflect the remaining spray plumes allows for the internal flow inside the nozzle to remain unaltered as it would be in the engine. However, the isolation shield may interact with the spray and change the aerodynamics slightly inside the spray chamber. In future work this injector will be used to perform engine testing and it is therefore desirable not to alter the injector when performing the X-ray testing.

2.4 Rate of injection measurements

To further understand the initial dynamics of the fuel spray, ROI studies were conducted using a Bosch ROI indicator (Bosch 1966). The ROI is not only important in understanding the spray dynamics, but is also essential for computational fluid dynamics (CFD) modeling as it provides boundary conditions for fuel injection into the combustion chamber.

Figure 4 shows a schematic of the ROI test rig used in the present study. Signals from the pressure transducer on the rate meter, the high-frequency pressure sensor on the oil rail, and a meter monitoring the current supplied to the injector solenoid were registered on a digitizing oscilloscope. In the present experiments, the injection ambient pressure was maintained constant at 3 MPa for all tests to simulate X-ray test conditions. The pressure signal from the ROI meter was low-pass filtered at 30 kHz and ensemble averaged over 512 traces. 3,750 injections were used to measure the total injected quantity for each condition, which is used to scale the ROI plots obtained. For both conditions the commanded fuel delivery was set to 100 mm^3 per stroke. Rate profiles were obtained for a range of oil rail pressures and injection deliveries. It is important to note that all six spray plumes were measured in the ROI experiments, while spray isolation was only used for the X-ray testing. For the work presented in this paper, it is assumed that an average of one-sixth the total fuel quantity is injected

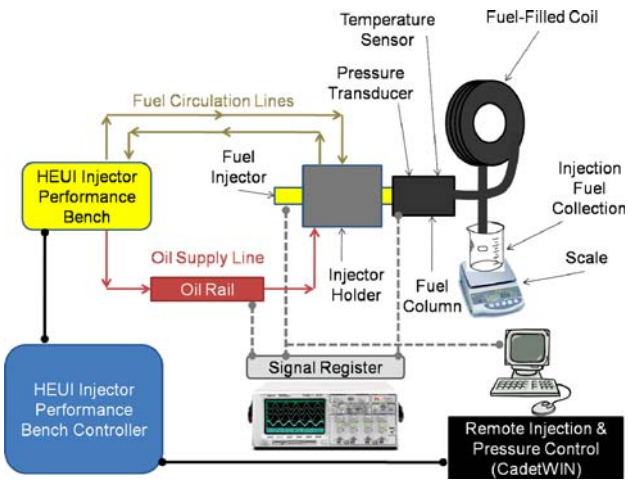

Fig. 4 Schematic of rate of injection (*ROI*) test setup

per orifice. This is done for comparisons with measurements taken with the X-ray studying only one of the six orifices.

2.5 X-ray radiography test conditions

Sprays in diesel engines encounter an environment of high pressure, temperature, and density. Unfortunately, it is not currently possible to replicate these conditions in an X-ray radiography experiment. The X-ray transparent windows used in these experiments are of polyimide film that cannot withstand high temperature. Nitrogen at room temperature was used as fill gas at 3 MPa pressure. Minimal evaporation of the fuel is expected to occur at these conditions. Expansion tubes were utilized on both of the X-ray windows to allow for elevated pressure in the spray chamber. Since the polyimide windows are the weakest points in the spray chamber, these tubes were attached to the windows as a safety precaution in the event of a rupture due to high pressures. The increased chamber pressure, and thus chamber density, along with the long path-length cause significant extinction of the X-rays. Therefore, increased number of averages was taken at each coordinate to improve the quality of the measurements. While the temperature and pressure levels in these experiments are far from those in a diesel engine, the density is 34.13 kg/m^3, which is comparable to engine density, an important parameter for fuel spray.

Two oil rail pressures were selected: 17 and 21 MPa, which correspond to peak injection pressures of about 110 and 135 MPa according to the injector pressure intensification ratio, 6.6, mentioned earlier. A fuel injection quantity of 100 mm^3/stroke was specified in the injector control software for both oil rail pressures. These parameters were used in the present study due to their consistency with known part-load turbo-charged heavy-duty engine test conditions. Table 1 lists other specific parameters of the experiments.

2.6 Numerical model

Standard models available with STAR-CD were used to perform simulations examining external spray from one orifice of the 6-hole nozzle. The gas phase is described using the Navier–Stokes equations in conjunction with RNG $k-\varepsilon$ turbulence model. The length and time scale for the spray is too small to be resolved; hence sub-grid scale modeling was necessary to describe the spray physics. Spray models used are Reitz and Diwakar model for atomization and droplet breakup (Reitz and Diwakar 1987), advanced collision model (Schmidt and Rutland 2000; Aamir and Watkins 1999), spray evaporation model (Ranz and Marshall 1952), standard turbulent dispersion model (Gossman and Ioannides 1983), RNG $k-\varepsilon$ turbulence model, and standard drag model (Liu et al. 1993). In addition, the injected fuel spray was represented by a stochastic system of a discrete number of parcels. These injected parcels were of the size of the nozzle orifice diameter with the injection velocity determined from ROI profile. Post-processing codes were written to calculate the liquid penetration and radial mass distributions at a given time. The computational domain simulating the spray chamber is of 50-mm diameter and 200-mm length. An O-mesh was generated with cells near the center forming a cube so that no acute angles are present between adjacent sides. This O-mesh is better than a radial mesh as used in previous STAR-CD simulations (Larmi et al. 2002) since it avoids narrow wedge-shaped cells near the center of the spray chamber. A mesh with 14 × 14 grids in the square and 14 × 56 in the circle outside was generated. 110 grid points were used in the direction of injection (+Z) and using a geometric distribution, the grids near the injector were 1 mm as shown in Fig. 5.

Table 1 X-ray radiography test conditions

Parameter	Quantity
Injection system	Caterpillar HEUI 315B
Number of orifices	6
Orifice diameter (μm)	169 with $L/D = 4.412$
Oil rail pressure (MPa)	Case 1: 17/case 2: 21
Oil temperature (°C)	60
Fill gas	Nitrogen (N_2)
Chamber density (kg/m^3)	34.13
Fuel	Viscor and cerium blend
Fuel temperature (°C)	40
Fuel injection quantity (mm^3/stroke)	100

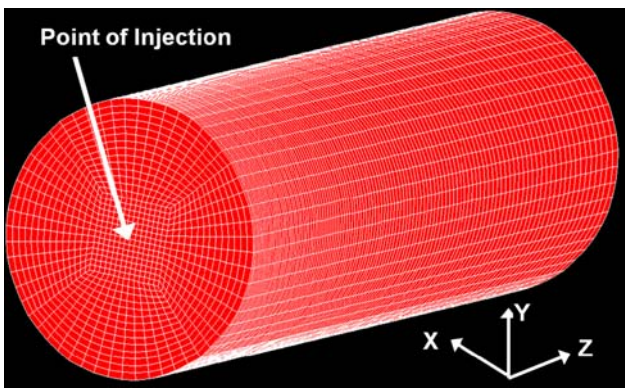

Fig. 5 Computational mesh

3 Results and discussion

3.1 Rate of injection

The ROI profiles for the oil rail pressures of 17 and 21 MPa are shown in Fig. 6. Both cases show similar delay between commanded start of injection (SOI) and apparent SOI, and have comparable rate shapes. As expected, the higher rail pressure yields a higher peak value of ROI with a slightly quicker initial rise than the 17 MPa case. A notable feature of both rate profiles is the slower rise to the "steady state" injection period than that with single-fluid, single-hole common rail injection systems (Naber and Siebers 1996). It should be mentioned that the ROI profiles shown are for a combination of all six orifices.

Using ROI profile for the early transition region ($t = 2.2$–2.4 ms), as shown in Fig. 6, as an input to the numerical model yields gross underprediction of penetration lengths in comparison to the X-ray data (cf. Fig. 8). Note that only one hole of the injector was studied using X-ray radiography, whereas all six were used with the rate meter. It has been shown in previous work that there is hole-to-hole variation seen in multi-hole nozzles (Wang et al. 2003; Warrick et al. 1996). Therefore, directly scaling the injection rate from six-sprays to a single spray in the transition region might cause this underprediction.

According to the control volume analysis in Kastengren et al. (2007a, b), X-ray radiography can be used to compute the total spray mass and hence ROI, until the spray has reached the downstream end of the measurement domain. This ROI computed from the X-ray data represents the activity of the single observed spray plume, rather than the behavior of all of the fuel exiting the injector. Figure 7a presents the ROI obtained from the X-ray data up to 0.15 ms at the first measurement location (0.283 mm). The lines represent a linear fit to the data.

We believe that the X-ray ROI measurements are potentially more reliable, because in the near-nozzle region, these measurements depend on a relatively simple physical process (X-ray absorption). The Bosch rate meter, in contrast, is based on the mass flow generating a quasi-one dimensional flow in a duct, which causes changes in the liquid pressure, which is measured a few centimeters from the nozzle and then correlated to ROI (Bosch 1966). Moreover, several artifacts can be seen in Bosch rate measurements including values less than zero immediately before SOI and oscillatory behavior near the end of

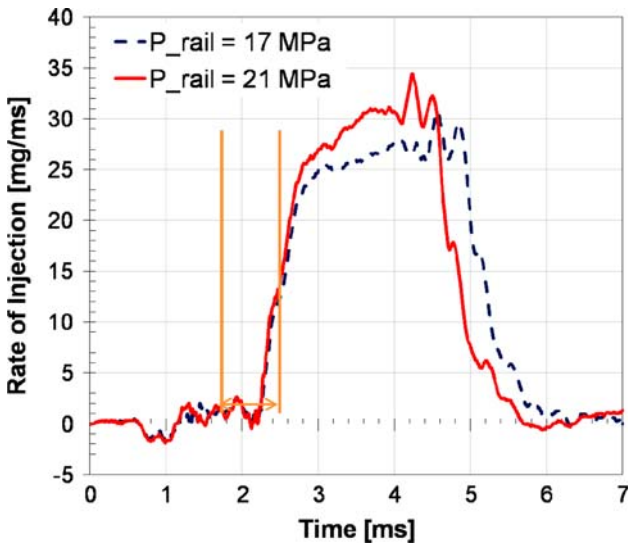

Fig. 6 Rate of injection profiles for 17 and 21 MPa oil rail pressures, 30 bar ambient pressure, 100 mm^3 per stroke fuel delivery. The transition period of rapid increase to quasi-steady injection is marked

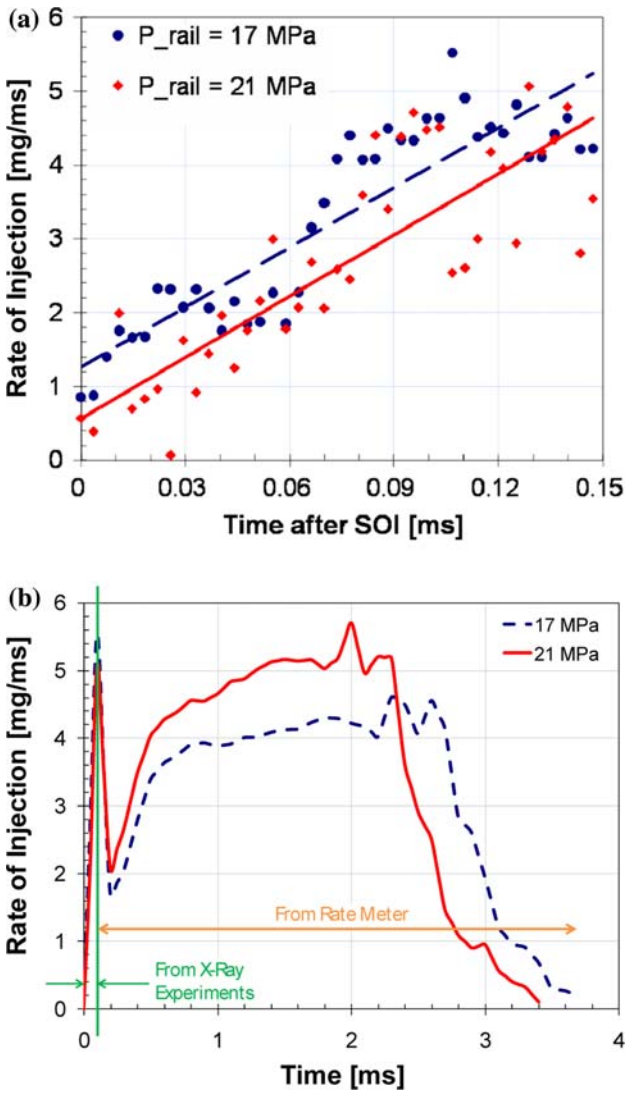

Fig. 7 **a** Rate of injection as measured from X-ray data for different rail pressures along with the respective linear fits. **b** Hybrid ROI profile of a single orifice used for input in numerical simulation

injection. Payri et al. (2008a, b) investigated the correction of rate profile measurements obtained from a Bosch fuel rate meter. In this study, a methodology was proposed to correct signal cumulative phenomenon that distorts the measured profile. Although the technique proposed could not be applied to the HEUI system, Payri's study indicates limitations of using the rate meter for ROI measurements. Other than random noise, the X-ray ROI does not suffer from these artifacts.

For the STAR-CD simulations, the initial ROI was obtained from X-ray data and was combined with the steady state ROI obtained from the Bosch meter to construct an injection rate for the duration of injection. The total mass injected through the single hole of the nozzle was one-sixth of the total mass injected. The hybrid ROI profile inputted into the numerical model is shown in Fig. 7b. The regions obtained from X-ray and from the rate meter are indicated on the plot.

3.2 Liquid penetration

Comprehensive data analysis was performed to investigate the near-nozzle spray characteristics using the X-ray radiography measurements. Liquid penetration was obtained by determining the time at which the leading edge of the fuel arrives at each axial location. This was done by recording the time at which the X-ray intensity decreases by a threshold value of 25%, indicating absorption by the fuel at each axial location in the experimental domain.

Figure 8 presents the measured and predicted liquid penetration lengths plotted versus time for oil rail pressures of 17 and 21 MPa. The scale is adjusted so that zero is the instant when the first amount of fuel is visible for each spray. There are several observations from this figure. For both rail pressures, a slow penetration region up to 0.1 ms is followed by a faster penetration region (where penetration scales linearly with time) up to 0.2 ms. The last measured point for the 17-MPa case suggests that the spray may be entering a region where penetration scales as square root of time; however, more measurements would be necessary to verify this trend. These spray penetration characteristics are consistent with the observations of previous researchers (Hiroyasu and Arai 1990; Naber and Siebers 1996).

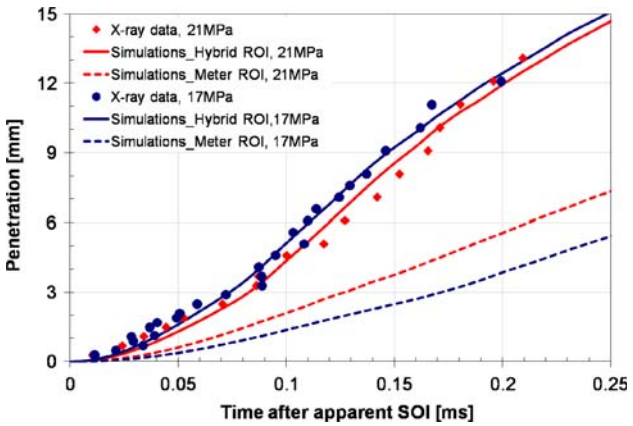

Fig. 8 Validation of spray models in STAR-CD against X-ray penetration data for oil rail pressures of 17 and 21 MPs, 30 bar ambient pressure, 100 mm^3/stroke fuel delivery. Predicted and measured (using ROI obtained from X-ray and rate meter) liquid penetration lengths are plotted versus time

Validation of STAR-CD simulations against penetration data is also presented in Fig. 8. The differences in penetration lengths resulting from the various ROI profiles can be clearly observed. When the profile from the rate meter is used in the simulations, the predicted penetration lengths are significantly smaller than those measured in X-ray experiments. Better agreement is observed when the ROI profile from X-ray data is mated with that from the rate meter (cf. Fig. 7b). In general there is an excellent match for both injection pressures, except for small differences observed earlier (<0.1 ms).

For the higher rail pressure case, the penetration speed increases more gradually and continues increasing throughout the measurements. For both pressures, the maximum speeds achieved are notably lower than those achieved at similar conditions with a single-hole injector (Kastengren et al. 2008). Further examination indicated that the single-hole injector with the single-fluid common rail injection system used in the cited study shows a much steeper rise in mass flow rate during the initial stage of injection than the HEUI system. This slower ramp in ROI for the HEUI system may account for the slower penetration speeds observed in the present experiments.

Another notable observation from Fig. 8 is that the higher oil rail pressure case shows lower penetration speeds than the lower oil rail pressure case for some parts of the spray. This is unexpected, since other studies indicate that a higher injection pressure usually yields faster penetration (Payri et al. 2008a, b; Kastengren et al. 2008). Moreover, correlations in the literature show that the penetration scales with the square root of the difference in the injection and ambient pressures (Payri et al. 2008a, b; Naber and Siebers 1996). The ROI profiles measured with the Bosch rate meter also indicate a faster rise in mass flow for the higher oil rail pressure. Figure 9 presents the projected liquid fuel density distributions at 0.122 ms after apparent SOI for the two pressure cases. As indicated, the penetration for the 21 MPa rail pressure case is smaller than for the lower pressure case during this transient period.

The slightly faster penetration for the lower rail pressure case is unexpected. It should be noted, however, that the current measurements have been performed closer to the nozzle than most penetration measurements in the literature

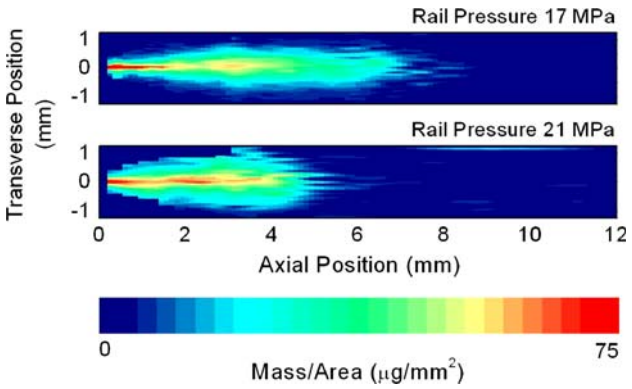

Fig. 9 Full field spray projected density versus axial position at 0.122 ms after SOI for 17 and 21 MPa oil rail pressures, 30 bar ambient pressure, 100 mm^3/stroke fuel delivery

and therefore cover a significantly shorter time than most penetration measurements. The penetration in this region depends highly on the needle motion and pressure buildup dynamics of the injector, which appear to be slower for the injection conditions at 21 MPa than at 17 MPa. The authors believe that this is due to needle and flow dynamics inside the injector for the particular injection conditions selected, rather than an artifact of the measurements, and that more extensive penetration measurements would follow the conventional trend of faster penetration with higher injection pressure. This also provides further evidence based on our X-ray measurements that the near-nozzle spray characteristics are very strongly influenced by internal injector dynamics, which is consistent with previous studies (Arcoumanis and Gavaises 1998; Gavaises et al. 2002).

The simulations also show a similar trend, i.e., the 17-MPa rail pressure case yields higher penetration speed compared to that for the 21-MPa rail pressure case. When only the data acquired from the rate meter are used for the ROI input, the simulations indicate that the higher oil rail pressure case yields a higher penetration. This is because the ROI for the early transition region is taken from the X-ray data. In the region this close to the nozzle, only the upstream conditions affect spray penetration rather than the details of the spray models. As seen in Fig. 7, the 17-MPa rail pressure case yields higher injection rates and thus higher injection velocities. This is the reason as to why the 17-MPa rail pressure case has faster penetration than the 21-MPa rail pressure case in both experiments and simulations.

Previous researchers have measured diesel spray penetration, and provided correlations for penetration behavior. Payri et al. (2008a, b) derived a correlation based on studies from a multi-hole nozzle, which is more representative of the injector used in the present study. He reported the following correlation in the transition region:

$$S = (0.018)(\rho_a)^{-0.256}(\Delta P)^{0.516}(t)^{1.044}. \quad (2)$$

The coefficients were obtained through curve fitting to match penetration length in the first 15 mm region of the spray. In the short-time limit, Naber and Siebers (1996) reported the following correlation:

$$S = C_v(t)\sqrt{\frac{2\times(P_f - P_a)}{\rho_f}}. \quad (3)$$

Figure 10 presents the X-ray data for rail pressure of 17 MPa and the above penetration correlations. For our case C_v was not measured. Extensive cavitation simulations (Som et al. 2009) yielded $C_v = 0.85$, which is comparable to typical values for diesel injection nozzles. Even if a smaller value of C_v were used, Fig. 10 indicates that the Naber and Siebers correlation predicts much higher penetration than the current data. This can be attributed to the fact that the initial gradient in the measured injection rate upon which the Naber and Siebers correlation is based is much higher than that in the current experiments. This yields high injection velocities earlier in the spray event, and hence faster penetration.

The penetration based on the Payri et al. (2008a, b) correlation is much closer to that obtained from the present X-ray data. It is important to note that this correlation was derived using a multi-hole nozzle, while Naber and Siebers (1996) used a single-hole nozzle. A closer comparison of the injection rates used by Payri et al. (2008a, b) and those used in the present study (cf. Fig. 6) shows that the injection rates are close to each other. However, the gradient in the ROI in Payri et al. (2008a, b) experiments was higher than that in the current experiments, resulting in a slight overprediction by the Payri et al. (2008a, b)

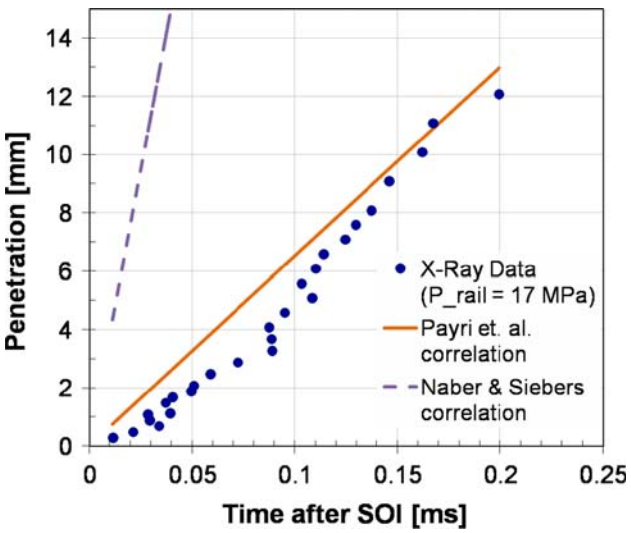

Fig. 10 Comparison of X-ray data at 17 MPa oil rail pressure with penetration correlations available in literature

correlation. Because of differences between the HEUI injection system and the injections systems used in the development of the aforementioned correlations, deviations are expected in the comparisons. In addition, the experiments presented here are in the near-nozzle region. Given the slower response time of the HEUI, it is not surprising that the data do not match the correlations very well.

For the 17-MPa case (cf. Fig. 8), downstream of $x = 12$ mm, simulations exhibit the long-time limit behavior (Naber and Siebers 1996) with the penetration length scaling with the square root of time. However, for the 21-MPa case this transition occurs at $x \approx 14$ mm. Naber and Siebers (1996) used a characteristic length (x^+) for this transition region, such that the penetration varies linearly with time upstream of this point (x^+), and as square root of time downstream of this point. They used the following equation for the characteristic length:

$$x^+ = \frac{d}{\alpha \tan(\theta/2)} \sqrt{\frac{\rho_f}{\rho_a}}. \tag{4}$$

Nozzle orifice diameter was 169 μm and α was assumed to be 0.66 (Naber and Siebers 1996). Optical cone angle was calculated as

$$\tan\left(\frac{\theta}{2}\right) = 0.31 \left(\frac{\rho_a}{\rho_f}\right)^{0.19}. \tag{5}$$

A value of about 13 mm was obtained for both the rail pressures, which is in good agreement with the value predicted by present simulations.

3.3 Fuel distribution

X-ray radiography has the unique capacity to obtain the liquid mass distribution in the spray. As previously mentioned, the measurement obtained by X-ray radiography is a measure of the density of the spray (in mass per unit volume) integrated over the path length of the beam, giving data in mass per unit area. Figure 11 presents a typical projected density profile in the transverse direction, obtained from X-ray measurements, at an axial position of 0.283 mm from the nozzle and 0.1 ms after SOI for the 21 MPa rail pressure case. The black rectangle at the bottom of the figure is provided to indicate the injector nozzle size (169 μm diameter). The projected density profile shows a Gaussian distribution even very near the nozzle. Other investigations using multi-hole nozzles show mass distribution profiles somewhat similar in shape to the system presented here; however, the spreading is less than that shown by the HEUI injection system (Leick et al. 2007; Malavé et al. 2006). Studies using single-hole common rail injectors have observed that close to the nozzle, the mass distribution has a more square shape and

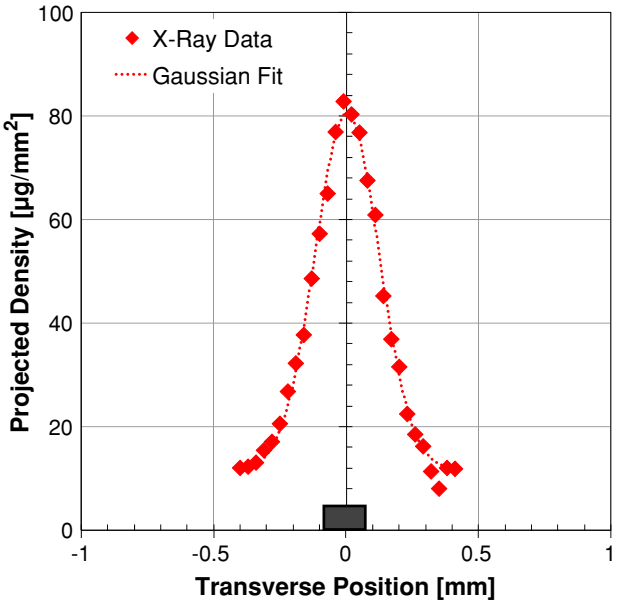

Fig. 11 Transverse mass distribution profile at axial position = 0.283 mm and 0.1 ms after SOI for the 21 MPa oil rail pressure case

develops to Gaussian distributions at further downstream locations (Kastengren et al. 2008).

Figure 12 presents X-ray measurements and simulations using STAR-CD in terms of the transverse projected density distribution at an axial position of 2.883 mm from the nozzle and 1.05 ms after SOI for the two pressure cases. Post-processing tool was developed to obtain results, which can be directly compared with the line-of-sight measurements from X-ray data. All the droplets at a given time in

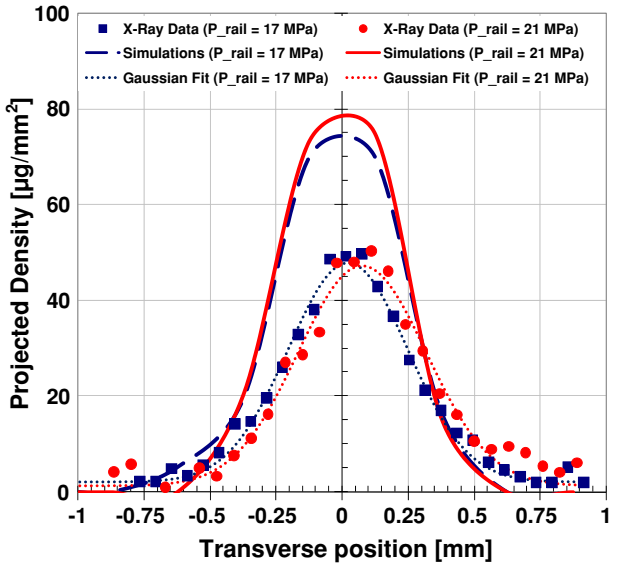

Fig. 12 Comparison of X-ray measurements and simulations using STAR-CD in terms of the transverse mass density distribution at an axial position 2.883 mm from the nozzle and 1.05 ms after SOI

the spray were projected to a two-dimensional plane. These droplets were then accounted for based on their axial and transverse location to obtain projected density profiles. Both the simulations and measurements exhibit Gaussian distributions for the two pressure cases. While simulations fairly reproduce the X-ray data qualitatively, the spray density is overpredicted for both the cases. This over-prediction yields a difference of peak mass value of about 40%, resulting in a 50% over-prediction of the transverse integrated mass (TIM) at the 2.883 mm axial location. However, the agreement becomes more satisfactory away from the center in the transverse direction for both the cases. In general, the comparison clearly indicates the need for additional work to further improve the spray models.

Figures 13 and 14 present mass distributions for the two pressure cases at 0.15 and 0.99 ms after SOI at various axial locations along the spray. Projected density contour plots are also shown for visualizing the spray at these times. At 0.15 ms after SOI, the two pressure cases exhibit similar mass distributions at the various axial locations. As can be expected, closer to the nozzle the projected density is significantly higher near the center of the spray, and then spreads out at downstream locations. Both the peak values and the width of the distributions at 0.15 ms after SOI are quite similar, with projected density peaks around 90 μg/mm^2 at the farthest upstream axial location. Later, in the spray event, i.e., 0.99 ms after SOI (cf. Fig. 14), more noticeable differences between the two pressure cases at 0.283 mm from the nozzle are found. However, further downstream, 2.483 and 7.083 mm from the nozzle, the distributions appear to be similar for the two rail pressures. Overall, for both times after SOI, the 17-MPa rail pressure spray exhibits a nearly symmetric distribution, while some asymmetry is observed for the 21-MPa rail pressure case. Also, the peak projected density for the 21-MPa spray is approximately 15% higher than that of the 17-MPa spray.

Integrating the mass distribution in the transverse direction yields the TIM at a given time and axial location. Figure 15 presents the computed TIM, based on the X-ray data, along the axial location at 0.15 ms and 0.99 ms after SOI for both the pressure cases. At 0.15 ms after SOI, the injection event is still in a transient stage and has not reached the end of the measurement domain, which is also indicated in Fig. 13b. Consequently, TIM increases with distance from the nozzle and then returns to zero. At 0.99 ms after SOI, TIM continuously increases with axial position along the axial location. This can be explained using the control volume analysis reported in previous work (Kastengren et al. 2007a, b, 2008), which obtained the mass-averaged axial velocity of the spray at any axial location using the following equation:

$$V_{\mathrm{ma}}(x_o, t) = \frac{\dot{m_{\mathrm{cv}}}(x > x_o, t)}{\mathrm{TIM}(x_o, t)}. \tag{6}$$

here V_{ma} is the mass-averaged axial velocity, and $\dot{m_{\mathrm{cv}}}$ is the mass flow rate across a cross section located at $x = x_{\mathrm{o}}$.

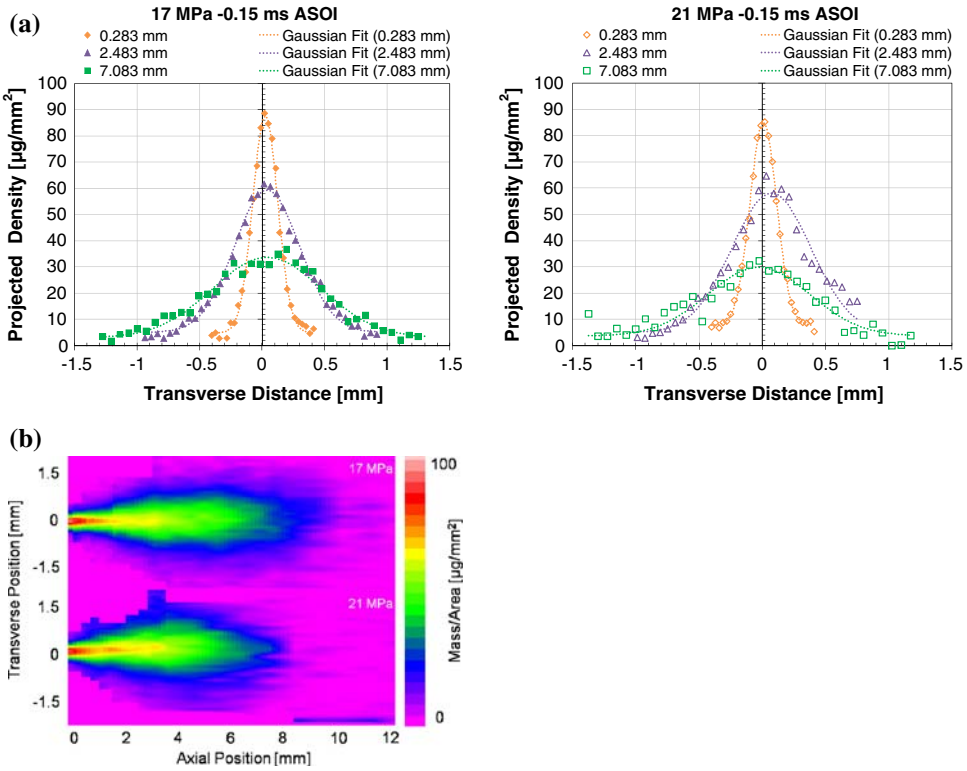

Fig. 13 **a** Transverse mass distributions at 0.15 ms after SOI for 17 and 21 MPa oil rail pressures plotted at axial positions of 0.283, 2.083, and 7.083 mm from the nozzle. **b** Full field spray projected density contours at 0.15 ms after SOI for oil rail pressures of 17 and 21 MPa

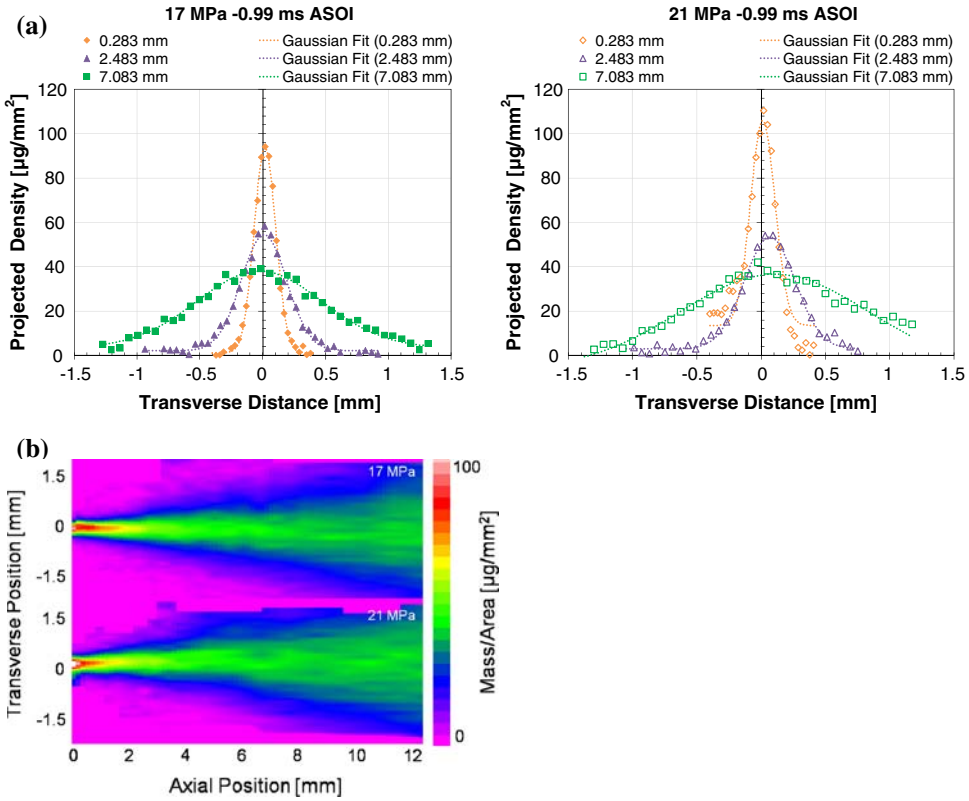

Fig. 14 **a** Transverse mass distributions at 0.99 ms after SOI for 17 and 21 MPa oil rail pressures plotted at axial positions of 0.283 mm, 2.083 mm, and 7.083 mm from the nozzle. **b** Full field spray projected density contours position at 0.99 ms after SOI for oil rail pressures of 17 and 21 MPa

Using this information, the mass-averaged axial velocity at any location normalized by the corresponding value at x_o can be determined using the following equation:

$$\frac{V_{\mathrm{ma}}(x = x_0, t)}{V_{\mathrm{ma}}(x = 0.283\,\mathrm{mm}, t)} = \frac{\mathrm{TIM}(x = 0.283\,\mathrm{mm}, t)}{\mathrm{TIM}(x = x_0, t)}. \quad (7)$$

Figure 15b presents the normalized axial velocity versus x_0 obtained using the above equation for the 17-MPa rail pressure case at 0.99 ms after SOI. The spray velocity decays quite rapidly in the downstream direction, decreasing to half its initial value in the first 5 mm of spray. These results are qualitatively consistent with the study of Roisman et al. (2007), who observed a strong dependence of the spray tip velocity on the ambient pressure, and a more rapid decrease in this velocity at higher ambient pressures.

3.4 Spray isolation

Figure 16 presents the variation of projected spray density with respect to the axial position. As seen in Fig. 16a, the two sprays exhibit similar structures initially (i.e., 0.7 ms after SOI). The 21-MPa rail pressure case shows interesting behavior near the nozzle starting around 0.9 ms after SOI. A broadened region of the spray appears during this time lasting approximately 0.73 ms (cf. Fig. 16b). Taking a closer look at the transverse mass distribution at the first measurement location (0.283 mm from the nozzle) at various times after SOI, a shift in mass distribution is observed as shown in Fig. 16c. At 0.7 ms after SOI (before the broadening is observed) the mass distribution is fairly symmetric. It then increases at the negative transverse locations at 0.9 ms after SOI, and increases near the positive values at 1.64 ms before it vanishes, and then the mass distribution is again even about the spray axis. This behavior suggests some hardware interference of the isolation shield with the spray of interest close to the nozzle tip.

Optical imaging was used to evaluate the effectiveness of the isolation shield. Visual inspection of the shield indicated that the hole-of-interest was unobstructed as seen in Fig. 3c. Nevertheless, interaction, if any, between the spray and the shield itself that may explain this anomalous penetration behavior and other interference observed in the X-ray experiments, was desired to be seen. Both oil rail pressures were tested; however, due to limitations imposed by the windows used for optical access, lower ambient pressure in the spray chamber was necessary. Figure 17 presents an image of an injection event for 17-MPa oil rail pressure, 0.2 MPa chamber pressure, and a fuel delivery of 100 mm^3/stroke. Although some accumulation of mass was observed on the slanted surface of the shield below the

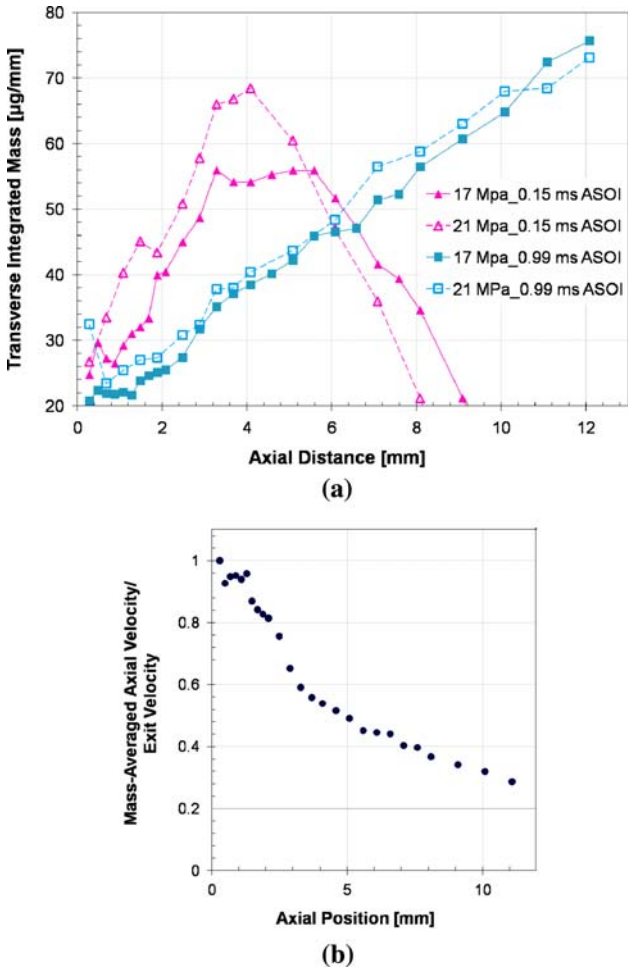

Fig. 15 **a** Transverse integrated mass (*TIM*) versus axial position at 0.15 and 0.99 ms after SOI for 17 and 21 MPa oil rail pressures. **b** Trend in mass-averaged axial velocity versus axial position at 0.99 ms ASOI for 17 MPa oil rail pressure

spray, no errant interference with the spray was observed. However, future improvements to the shield design would include a more drastic slope on the angled surface.

3.5 Cone angle

The spray cone angle is computed from X-ray measurements by measuring the FWHM of Gaussian fits to the transverse mass distributions at each axial location and time step in the measurements. The cone angle is then calculated from a linear fit to the FWHM locations, and plotted as a function of time in Fig. 18a. If the transverse mass distribution were perfectly axisymmetric and Gaussian, this cone angle value would define a volume containing half the total mass in the spray. By definition, using the FWHM to compute cone angle, X-ray radiography focuses on the core of the spray, while optical techniques focus on the spray periphery. Thus, the X-ray

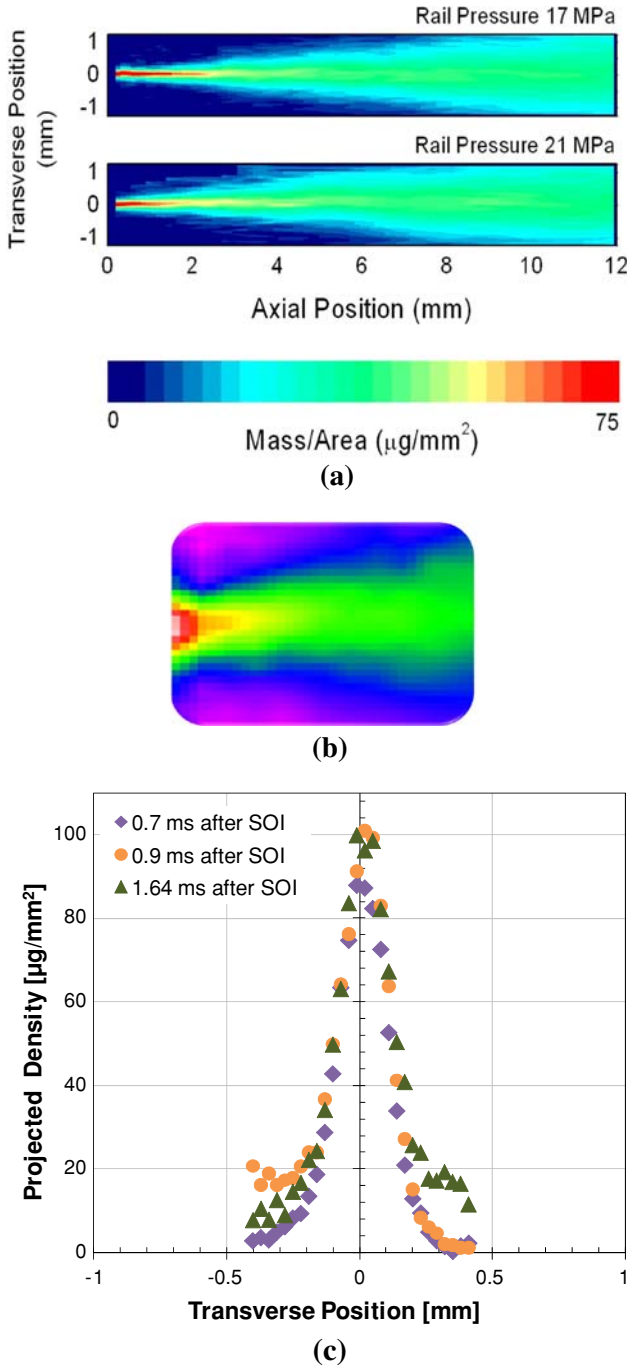

Fig. 16 **a** Full field mass projected density at 0.7 ms after SOI for rail pressures of 17 and 21 MPa. **b** Projected density contours in the near-nozzle region at 1.15 ms after SOI for the 21-MPa rail pressure case. **c** Transverse mass distribution at axial position of 0.283 mm from the nozzle at three different times after SOI for the 21-MPa rail pressure case

cone angle is expected to be smaller than the optical cone angle (Ciatti et al. 2004).

Although there is no noticeable difference in the cone angle values between the two rail pressures, the cone angle tends to be higher for the 21-MPa rail pressure case than

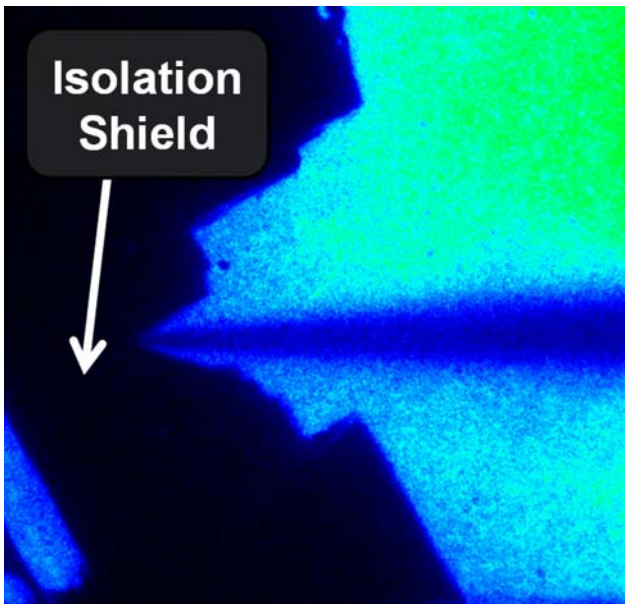

Fig. 17 Optical image of injection event for oil rail pressure of 17 MPa, chamber pressure of 2 bar, and fuel delivery of 100 mm^3/stroke

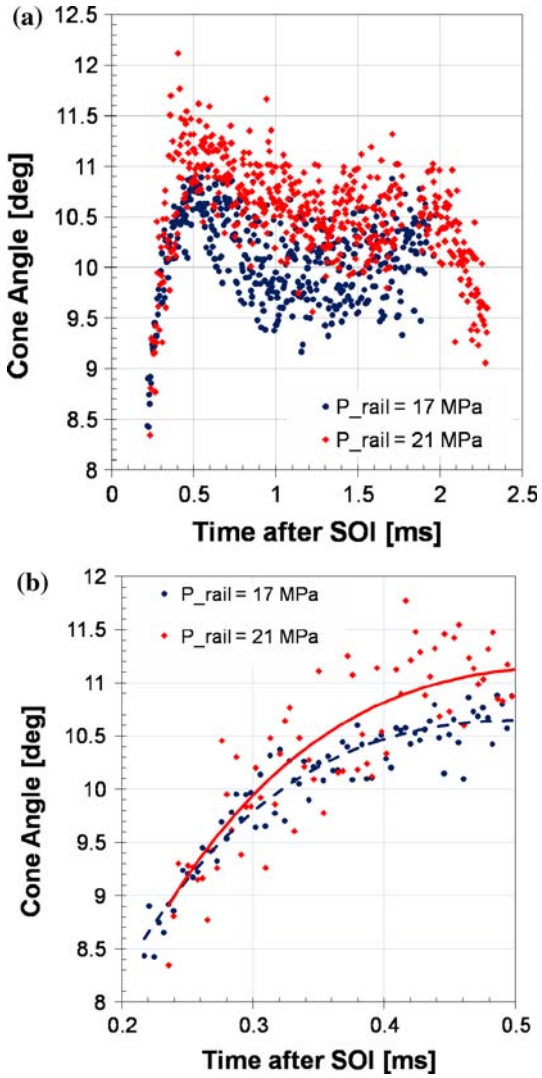

Fig. 18 **a** Measured cone angle versus time for 17 MPa and 21 MPa oil rail pressures. **b** Zoomed cone angle versus time during the initial transition period

that for the 17-MPa case, with average quasi-steady state values of 10.5° and 9.9°, respectively. Figure 18b presents the cone angle versus time in the initial transient part of the spray along with a polynomial fit to the data. The spray cone angle for the 21-MPa rail pressure case is consistently larger compared to that of the lower pressure case in this transient region as well. This is consistent with the projected density results discussed earlier in the context of Fig. 9, which presented the projected density for both sprays during the transient period of injection. These cone angle values are higher than those observed for single-hole common rail injectors under similar conditions (Kastengren et al. 2008). Internal flow dynamics are significantly different between multi-hole and single-hole nozzles. For multi-hole nozzles, the fuel undergoes a change in flow direction, which increases cavitation and turbulence, and thus causes broader cone angle. In single-hole nozzles, there is less motion of the fuel upstream of the nozzle exit, resulting in less cavitation and smaller cone angle.

4 Conclusions

Sprays from an unaltered tip of a production HEUI injector were investigated at engine-like ambient density using X-ray radiography for two oil rail pressures. Spray characteristics in terms of the fuel penetration, spray mass distribution, mass-averaged axial spray velocity, and cone angle were reported.

Rate of injection testing was also performed to supplement the X-ray experiments. The ROI profile from the rate meter exhibited a slow initial rise compared to that from X-ray measurements during the transient stages of injection. Using ROI profile from the rate meter yielded gross underprediction in the simulations. Consequently, the X-ray radiography data are judged to be a more accurate measure of ROI when fed as input to the simulations.

Although a direct comparison cannot be made between the performance of the HEUI dual-fluid multi-hole injection system and common rail single-fluid, single-hole injection system, on a bulk level they show several dissimilarities. Naturally, the differences in fluid dynamics of a single and multi-hole injector contribute to these differences. In addition, some of these could be attributed to dissimilarities in the initial transient rise in ROI between the two systems.

Measurements were used for the validation of spray atomization and dispersion models in STAR-CD software. Simulations indicated good agreement with experiments in terms of the fuel penetration. While the trends in mass distribution were captured, simulations noticeably underpredict the transverse projected density profiles, demonstrating the need for improved spray models in the near-nozzle region.

Some anomalous behavior was observed regarding penetration in that the lower oil rail pressure case exhibited faster penetration than the higher rail pressure case. Further analysis suggested that this is due to the slower pressure build-up in the injector, which can be attributed to the needle and flow dynamics inside the injector, for the latter case. Detailed analysis based on the mass distribution measurements in the region close to nozzle exit also indicated some spray broadening for the higher rail pressure case, implying some interference of neighboring sprays. While optical images of the spray indicated that the shield performed effectively, improvements will be made for subsequent measurements.

To the best of our knowledge, this is the first time that quantitative measurements of sprays using X-ray radiography have been obtained from a single plume of a 6-hole, full production nozzle at realistic engine-like densities.

Acknowledgments This work is supported by the US Department of Energy Office of Vehicle Technology under the management of Gurpreet Singh. The experiments were performed at the 1-BM beamline of the APS. Use of the APS is supported by the US Department of Energy under contract DE-AC02-06CH11357. The authors would like to thank Rick Zadoks and Robert McDavid from Caterpillar Inc. and Anthony Dennis from Test Development Innovators L.L.C. for their help.

References

Aamir MA, Awais MM, Watkins AP, Lockwood FC (1999) CFD and neural network modelling of dense propane spray. In: Proceedings of the 15th ILASS-Europe annual conference

Arcoumanis C, Gavaises M (1998) Linking nozzle flow with spray characteristics in a diesel fuel injection system. Atomization Sprays 8(3):307–347

Arcoumanis C, Cossali E, Paal G, Whitelaw JH (1990) Transient characteristics of multi-hole diesel sprays. SAE Paper 900480

Bosch W (1966) The fuel rate indicator: a new measuring instrument for display of the characteristics of individual injection. SAE Paper 660749

Chaves H, Knapp M, Kubitzek A, Obermeier F, Schneider T (1995) Experimental study of cavitation in the nozzle of diesel injectors using transparent nozzles. SAE Paper 950290

Cheong SK, Liu J, Shu D, Wang J, Powell CF (2004) Effects of ambient pressure on dynamics of near-nozzle diesel sprays studied by ultrafast X-radiography. SAE Paper 2004-01-2026

Ciatti SA, Powell CF, Cheong SK, Liu J, Tanner FX (2004) Comparison of X-ray based fuel spray measurements with computer simulation using the CAB model. CIMAC congress. Kyoto, Japan

Gavaises M, Arcoumanis C, Roth H, Choi YS, Theodorakakos A (2002) Nozzle flow and spray development from VCO diesel injector nozzles. In: Thiesel conference on thermo and fluid dynamic processes in diesel engines. Valencia, Spain

Gavaises M, Tonini S, Arcoumanis C (2006) Prediction of liquid and vapor penetration of high pressure diesel sprays. SAE Paper 2006-01-0242

Giannadakis E, Gavaises M, Arcoumanis C (2008) Modelling of cavitation in diesel injector nozzles. J Fluid Mech 616:153–193

Glassey SF, Stockner AR, Flinn MA (1993) Development of the HEUI fuel injection system—integration of design, simulation, test, and manufacturing. SAE Paper 930271

Han J-S, Lu P-H, Xie X-B, Lai M-C, Nenein N (2002) Investigation of diesel spray primary break-up and development for different nozzle geometries. SAE Paper 2002-01-2775

Hiroyasu H, Arai M (1990) Structures of fuel sprays in diesel engines. Trans SAE 99(3):1050–1061

Kastengren AL, Powell CF, Cheong SK, Wang Y, Im KS, Liu Xin, Wang J (2007a) Determination of diesel spray axial velocity using X-ray radiography. SAE Paper 2007-01-0666

Kastengren AL, Powell CF, Wang Y-J, Wang J (2007b) Study of diesel jet variability using single-shot X-ray radiography. In: Proceedings of the ASME internal combustion engine division, Charleston, USA, October 2007

Kastengren AL, Powell CF, Wang Y, Im KS, Wang J (2008) X-ray radiography measurements of diesel spray structure at engine-like ambient density. In: Proceedings of the 21st ILASS annual conference, Orlando, FL, May 2008

Larmi M, Rantanen P, Tiainen J, Kiijarvi J, Tanner FX, Zarling KS (2002) Simulation of non-evaporating diesel spray and verification with experimental data. SAE Paper 2002-01-0946

Leick P, Reidel T, Bittlinger G, Powell CF, Kastengren AL, Wang J, Wang J (2007) X-ray measurements of the mass distribution in the dense primary break-up region of the spray from a standard multi-hole common-rail diesel injection system. In: Proceedings of the 21st ILASS-Europe meeting

Liu AB, Mather DK, Reitz RD (1993) Effects of drop drag and breakup on fuel sprays. SAE Paper 930072

Malavé A, Farrell P, Powell CF, Cheong S-K, Wang J (2006) Near-nozzle diesel spray imaging using X-rays. In: Proceedings of 19th annual conference on liquid atomization and spray systems

Montgomery DR, Chan M, Chang CT, Farrell PV, Reitz RD (1996) Effect of injector nozzle hole size and number spray characteristics and the performance of a heavy duty D.I. diesel engine. SAE Paper 962002

Mulemane A, Han J-S, Lu P-H, Yoon S-J, Lai M-C (2004) Modeling dynamic behavior of diesel fuel injection systems. SAE Paper 2004-01-0536

Naber JD, Siebers DL (1996) Effects of gas density and vaporization on penetration and dispersion of diesel sprays. SAE Paper 960034

Payri R, Salvador FJ, Gimeno J, Morena J (2008a) Macroscopic behavior of diesel sprays in the near-nozzle field. SAE Paper 2008-01-0929

Payri R, Salvador FJ, Gimeno J, Bracho G (2008b) A new methodology for correcting the signal cumulative phenomenon on injection rate measurements. Experimental techniques, January/February 2008

Pierpont DA, Reitz RD (1995) Effects of injection pressure and nozzle geometry on D.I. diesel emissions and performance. SAE Paper 950604

Powell CF, Yue Y, Poola R, Wang J, Lai MC, Schaller J (2001) X-ray measurements of high pressure diesel sprays. SAE Paper 2001-01-0531

Powell CF, Yue Y, Cheong S-K, Narayanan S, Cuenca R, Ciatti SA, Shu D, Wang J (2003) Effects of ambient pressure on fuel sprays

as measured using X-ray absorption. In: Proceedings of the 16th ILASS annual conference, Monterey, CA, May 2003
Ranz WE, Marshall WR (1952) Evaporation of drops. Chem Eng Prog 48(3):141–145
Reitz RD, Diwakar D (1987) Structure of high-pressure fuel sprays. SAE Paper 870598
Roisman IV, Araneo L, Tropea C (2007) Effect of ambient pressure on penetration of a diesel spray. Int J Multiphase Flow 33:904–920
Schmidt DP, Rutland CJ (2000) A new droplet collision algorithm. J Comput Phys 164:62–80
Siebers DL (1998) Liquid-phase fuel penetration in diesel sprays. SAE Paper 980809
Som S, Ramírez AI, Aggarwal SK, El-Hannouny EM, Longman DE (2009) Investigating the nozzle flow and cavitation characteristics in a production diesel injector. J Eng Gas Turbine Power (submitted)
Soteriou C, Andrews R, Smith M (1995) Direct injection diesel sprays and the effect of cavitation and hydraulic flip on atomisation. SAE Paper 950080
Stockner AR, Flinn MS, Camplin FA (1993) HEUI—a new direction for diesel engine fuel systems. SAE Paper 930270
Tanner FX, Feigl KA, Ciatti SA, Powell CF, Cheong SK, Liu J, Wang J (2004) Analysis of X-ray-based computer simulations of diesel fuel sprays. In: Proceedings of the 17th ILASS-Europe annual conference, Arlington, USA, May 2004
Tanner FX, Feigl KA, Ciatti SA, Powell CF, Cheong SK, Liu J, Wang J (2006) The structure of high-velocity dense sprays in the near-nozzle region. Atomization Sprays 16:579–597
Wang T-C, Han J-S, Xie X-B, Lai M-C, Henein NA (2003) Trans ASME
Warrick CB, Su TF, Farrell PV (1996) Temperature effects on fuel sprays from a multi-hole nozzle injector. SAE Paper 962005
Yudanov SV (1995) Hydraulically activated electronically controlled unit injector for diesel engines. SAE Paper 952057
Yue Y, Powell CF, Poola R, Wang J, Schaller J (2001) Quantitative measurements of diesel fuel spray characteristics in the near-nozzle region using X-ray absorption. Atomization Sprays 11:471–490